Article

# Engineering of Mesoporous Cube-like In$_2$O$_3$ Products as Ethanol Detection Platform at Low Operating Temperature: Effects of Different Transition Metals as Dopant Ions

Mosima B. Kgomo, Hendrik C. Swart, and Gugu H. Mhlongo*

Read Online

ACCESS | ▐ Metrics & More | ▐ Article Recommendations

**ABSTRACT:** Although most semiconductor metal oxides including In$_2$O$_3$ show acceptable sensitivity to volatile organic compounds, it is difficult to detect ethanol effectively at low operating temperatures and detection levels. In this study, pure and Co-, Ni-, and Cu-doped In$_2$O$_3$ products with their doping content maintained at 1 mol % were successfully produced using a hydrothermal approach. Explicit contrast on the structural, microstructural, and textural properties of the synthesized In$_2$O$_3$ products was examined to determine their gas sensing performance. The Cu-doped In$_2$O$_3$ sensor demonstrated improved response of 15.3 to 50 ppm ethanol and has satisfactory selectivity, stability, low detection limit of 0.2, humidity resistance, and decreased working temperature of 80 °C compared to 150 °C of the pure In$_2$O$_3$ sensor. This optimal gas sensing performance is derived from the cube-like morphology assembled with interlinked nanoparticles, which favors trapping more target gas molecules and exposing more active sites, thereby greatly improving its sensing ability. This study showed that the Cu-doped In$_2$O$_3$ sensor with 1 mol % is suitable for monitoring ethanol gas for food safety applications.
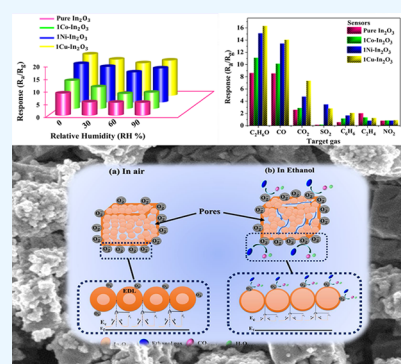
## 1. INTRODUCTION

Owing to their simple electrical measurements, capabilities in monitoring combustible hazardous gases, and diverse applications in the gas sensing field, nanostructured semiconducting metal oxide (SMO) based gas sensors have extensively been exploited by scientists worldwide. Among various kinds of SMO based gas sensors, the n-type In$_2$O$_3$ with electrons as density charge carriers has attracted much interest as an active sensor material due to its beneficial features of possessing a wide direct bandgap (3.55−3.75 eV)[1,2] high electrical conductivity, and intrinsic oxygen vacancies.[3] It can also monitor oxidizing gases such as nitrogen dioxide[4,5] and chlorine[6] and reducing volatile organic compounds (VOCs) such as acetone[7] and ethanol,[8] just to mention a few.

Ethanol finds applications in many sectors such as the food industry, healthcare, and chemical industries. In the food industry, the accumulation of ethanol in milk or fruits such as guava and mango can serve as an indicator for freshness level,[8−10] while on peaches and oranges ethanol can indicate the ripeness level.[11,12] In the healthcare, ethanol can act as a indicator for liver illnesses related to obesity which are produced by pathogens.[14] On the other hand, industries such as research councils use ethanol as an organic synthesis reactant or as a solvent.[15] But, ethanol can be susceptible to chemical combustion by reacting with oxidants, yet flammable at elevated temperatures.[13,14] As a VOC, ethanol can vaporize in the atmosphere and accumulate in high concentrations, thus,

making human beings vulnerable to its exposure. Adverse health effects such as ataxia, narcosis, and respiratory issues can be experienced when there is exposure to concentration levels greater than 1000 ppm for more than 8 h.[16−19] In addition, the intake of ethanol as a recreational beverage can cause traffic accidents owing to an adverse impact on a human being's consciousness. Considering social, environmental, and health safety, it is therefore pertinent and desirable to construct a highly stable, selective, and sensitive ethanol gas sensor.

Nanostructured In$_2$O$_3$ has demonstrated its potential in detecting VOCs such as ethanol. For example, Nguyen et al.[8] demonstrated a superior ethanol gas sensor exhibiting a maximum response of 85 toward 100 ppm of ethanol gas at 300 °C. Song et al.[20] reported on porous In$_2$O$_3$ nanospheres displaying an enhanced response value of 20 to 100 ppm at 275 °C. Even though pure In$_2$O$_3$ sensors can produce high responses to ethanol vapor, the high working temperatures can cause ethanol to be flammable, resulting in catastrophic damage to the sensor. Pure In$_2$O$_3$ based nanosensors operating at lower working temperatures are considered to be more
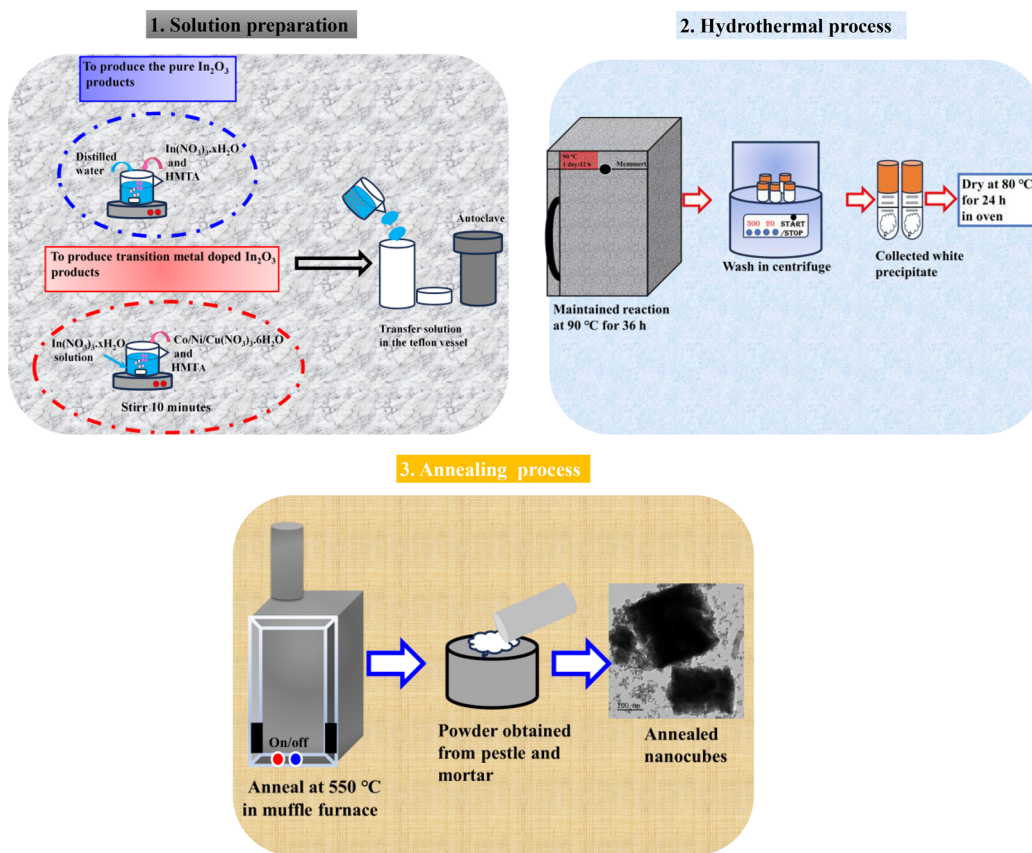
**Figure 1.** Schematic demonstration of the hydrothermal process to synthesize the pure and $1Co-In_2O_3$, $1Ni-In_2O_3$, and $1Cu-In_2O_3$ products.

energy efficient owing to their low power consumption, which leads to an increase of their lifespan. Previous findings have demonstrated that gas nanosensors operating at lower working temperatures are significantly needed in industries in which low power consumption and portability are a priority. For instance, in the fruit sector, the monitoring of gases emitted by fruits while being transported from one place to another is of importance as it requires portable gas nanosensor. In accordance with the literature, poor sensitivity and selectivity have been experienced by pure $In_2O_3$ based nanosensors operating at higher working temperature. Zhang et al.[21] reported on ethanol detection using particle-like $In_2O_3$ nanostructures which operated at 320 °C. While Elouali et al.[22] demonstrated ethanol gas sensing performance at 300 °C using $In_2O_3$ nanoparticles. On the other hand, Sun et al.[23] demonstrated ethanol detection at 220 °C using $In_2O_3$ nanospheres. Apart from high working temperatures, poor selectivity and short-term stability are also drawbacks experienced by the $In_2O_3$ sensor in its pure form. To overcome these drawbacks, the transition metal-ion doping approach can be adopted to efficiently reduce the working temperature and improve selectivity, sensitivity, and stability of the pure $In_2O_3$ sensor.

Transition metal-ions such as Cu, Ni, Co, and Fe have demonstrated to proficiently enhance the gas sensing performance of the pure $In_2O_3$ sensor by inducing inhibition of grain growth, which can produce the specific surface area.[24] For example, Chen et al.[2] revealed an improved ethanol gas sensor displaying a response value of 133 and rapid response/recovery times of 15/55 s at 350 °C using mesoporous Fe-doped $In_2O_3$ nanospheres. The improved gas sensing performance was

attributed to high specific surface area of 109.73 $m^2/g$. Zhang et al.[25] also demonstrated enhanced methane gas sensing characteristics of porous $In_2O_3$ microspheres with Ni-doping and ascribed the enhancement to high porosity and large surface area 42 $m^2/g$ of $In_2O_3$ microspheres which favored methane gas adsorption. Yong et al.[26] reported on improved ethanol gas sensor using Co-doped $In_2O_3$ hexagonal cylinder and attributed the improvement to a porous structure which enabled ethanol gas diffusion and large specific surface area 46.5 $m^2/g$ thus providing abundant reactive centers for ethanol vapor adsorption. On the other hand, Zhang et al.[27] presented excellent hydrogen sulfide gas sensing properties based on a hollow fiber-like Cu-doped $In_2O_3$ sensor at 6 mol % content which was ascribed to large surface area of 71.6 $m^2/g$. Based on these previous findings, transition metals incorporated as dopant ions can effectively modify pure $In_2O_3$ gas sensing properties. Therefore, it can be anticipated that doping with a suitable amount of Co, Ni, or Cu content into the $In_2O_3$ lattice can inhibit grain growth and give rise to a large specific surface area in which abundant active centers for gas adsorption can be produced resulting in improved gas sensing properties.

On another note, three-dimensional (3-D) nanocubes (NC) embedded with intertwined nanoparticles with mesoporous features can induce enhanced gas sensing characteristics owing to mesoporous structure features and large surface area, thereby offering reactive centers for target gas molecules to be adsorbed.[28] For this reason, tremendous research has been dedicated to the synthesis and characterization of NC-based SMO sensors.[29−3233] For example, Lu et al.[34] demonstrated porous $CO_3O_4$ nanocubes for ethanol monitoring. While Hai et al.[35] produced $\gamma$-$Fe_2O_3$ porous nanocubes via a hydro-
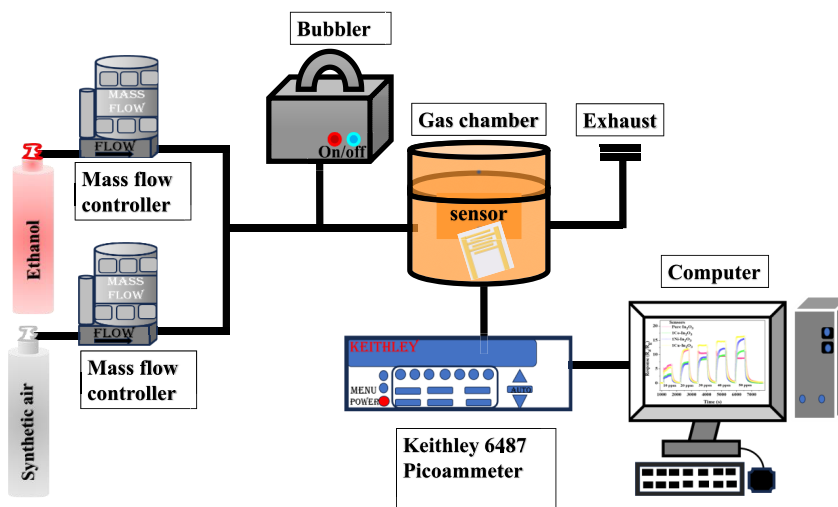
**Figure 2.** Diagram of the gas sensing station utilized to probe the sensing conduct of the pure and $1Co-In_2O_3$, $1Ni-In_2O_3$, and $1Cu-In_2O_3$ sensors.

thermal approach for excellent detection of both acetone and ethanol gas. The pronounced gas sensing characteristics of the two reported studies were explained by the 3-D morphology, which offered more channels for the target gas to be adsorbed and desorbed.

Therefore, to take an advantage of excellent properties possessed by the 3-D mesoporous nature of $In_2O_3$ structural features while exploring the influence of incorporation of transitional metals as dopant ions, this study investigated the high detection capabilities induce by Co/Ni/Cu-doped $In_2O_3$ as a detection platform for ethanol at lower detection levels and operating temperatures. The sensing performance was correlated with the structure, morphology, structural defects, and textural properties of the cube-like $In_2O_3$ products, and a sensing mechanism was generated.

## 2. EXPERIMENTAL SECTION

**2.1. Synthesis of the Pure, Co, Ni, Cu-Doped $In_2O_3$ Nanocubes.** The pure $In_2O_3$ and Co, Ni, Cu $In_2O_3$ products at 1 mol % doping level were produced via the facile hydrothermal method as demonstrated in Figure 1. In a normal experimental approach, the $Ni(NO_3)_2·6H_2O$, $Co(NO_3)_2·6H_2O$, $Cu(NO_3)_2·6H_2O$, hexamethylenetetramine (HMTA), $In(NO_3)_3·xH_2O$, and distilled water were utilized as starting materials. The following steps were carried out to fabricate the pure $In_2O_3$ products: $In(NO_3)_3·H_2O$ weighing 2 g was added to 40 mL of distilled water and was continuously stirred magnetically for 5 min. Meanwhile, 1.4 g of HTMA was added separately to a solution consisting of 10 mL of distilled water, and this mixture was constantly stirred for 5 min. Thereafter, the solution consisting of HTMA was added to the $In(NO_3)_3·xH_2O$ precursor solution under uniform stirring for 10 min at room temperature until reaching a colorless solution. This colorless solution was then transferred to a 200 mL Teflon vessel which was placed inside a stainless steel autoclave and was maintained in the oven at 90 °C for 36 h. After completion of the reaction, the solution was left to cool until it reached room temperature. By using the centrifuge, the resultant precipitate was collected and washed with ethanol and distilled water repeatedly for elimination of undesirable impurities. The final collected precipitate was dried in an oven for 24 h at 80 °C.

To prepare 1 mol % Co, Ni, and Cu-doped $In_2O_3$ products, the same experimental approach was used, however, with some modifications. In particular, a specific amount of the $Ni(NO_3)_2·6H_2O$, $Co(NO_3)_2·6H_2O$, $Cu(NO_3)_2·6H_2O$, needed to produce 1 mol % of Co, Ni, and Cu-doped $In_2O_3$ products was dissolved in 5 mL of distilled water and mixed with the prepared $In(NO_3)_3·xH_2O$ precursor solution while stirring for 5 min until a homogeneous solution was obtained. The resultant precipitate was collected by centrifugation, washed with water and ethanol repeatedly, and finally placed in an oven for 24 h at 80 °C. All dried precipitates were annealed in the furnace at 550 °C for 2 h to acquire the pure and 1 mol % Co, Ni, and Cu-doped $In_2O_3$ products. The obtained $In_2O_3$ product without dopant ions was labeled as the pure $In_2O_3$, while the Co, Ni, and Cu-doped $In_2O_3$ products at 1 mol % are represented as $1Co-In_2O_3$, $1Ni-In_2O_3$, and $1Cu-In_2O_3$ products, respectively.

**2.2. Characterization of the Pure and $1Co-In_2O_3$, $1Ni-In_2O_3$, and $1Cu-In_2O_3$ Products.** The X-ray diffraction (XRD) Panalytical X'pert PRO PW3040/60 equipped with radiation source $Cu/K\alpha$ ($\lambda$ = 1.5405 Å) was utilized to evaluate structural properties of the pure and $1Co-In_2O_3$, $1Ni-In_2O_3$, and $1Cu-In_2O_3$ products. The morphological and microstructural features were examined by a ZEISS-AURIGA field emission-scanning electron microscope (FE-SEM) and JEOL HR-TEM-2100 high-resolution transmission electron microscope, respectively. The surface area and pore diameter analyses were performed utilizing the Brunauer–Emmett–Teller (BET) and Barrett–Joyner–Halenda (BJH) methods on a Micromeritics TRISTAR 300 surface area analyzer. The Horiba Quantamaster spectrometer was used to obtain photoluminescence (PL) spectra under an excitation wavelength of 325 nm.

**2.3. Fabrication and Gas Sensing Testing of the Pure, $1Co-In_2O_3$, $1Ni-In_2O_3$, and $1Cu-In_2O_3$ sensors.** To fabricate the pure and $1Co-In_2O_3$, $1Ni-In_2O_3$, and $1Cu-In_2O_3$ sensors, 40 mg of each product was mixed with ethanol to form a thixotropic paste. The produced paste was drop-coated evenly onto an alumina sensor strip with interdigitated Pt electrodes and a Pt thermal heater at the back side. The sensors were heated to 300 °C to remove organic solvents and vapors. As illustrated in Figure 2, evaluation of the gas sensing
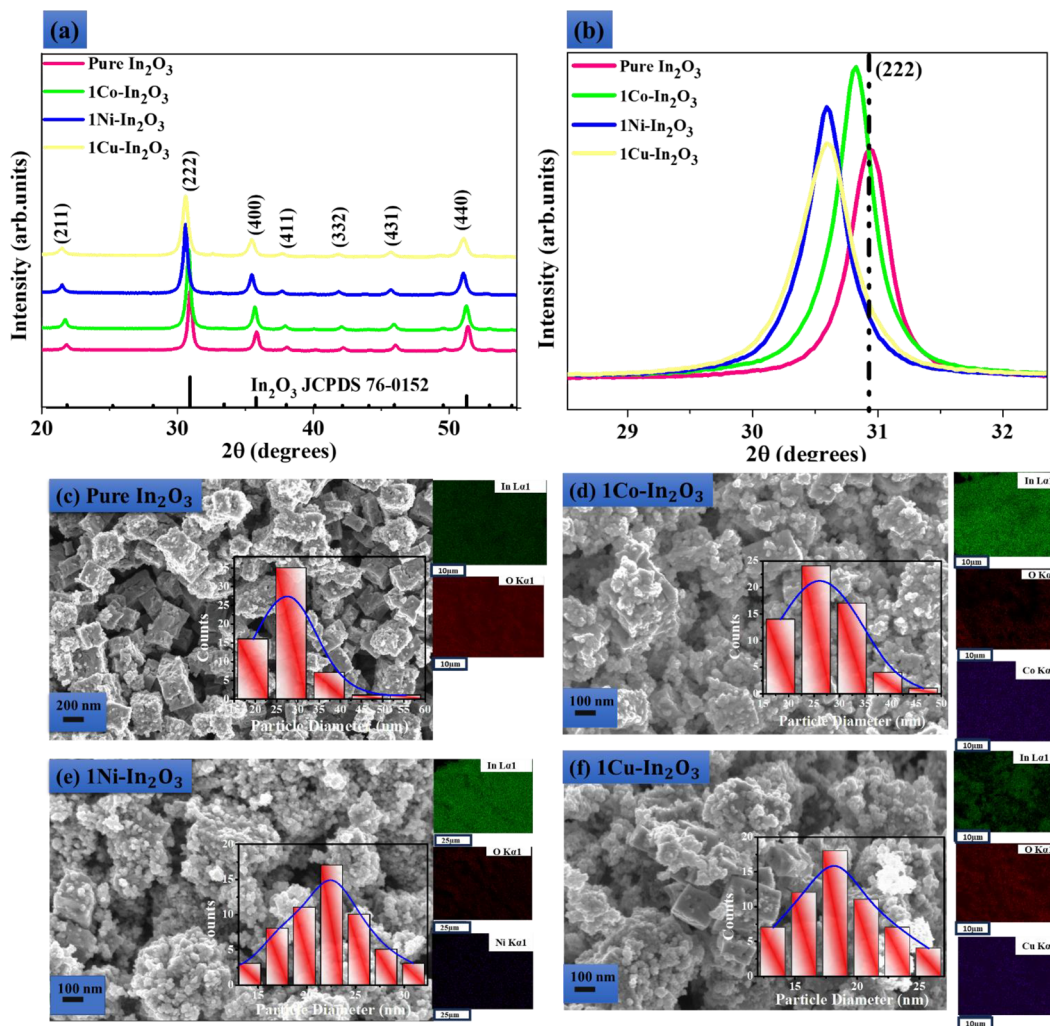
**Figure 3.** (a) XRD patterns of (b) magnified diffraction peak associated with the (222) plane, (c)-(f) SEM images, particle size distribution, and EDS elemental maps of the pure and $1Co-In_2O_3$, $1Ni-In_2O_3$, and $1Cu-In_2O_3$ products.

behavior of all fabricated $In_2O_3$ sensors was performed using a KSGAS6S (KENOSISTEC, Italy) gas sensing station at various working temperatures ranging from 20 to 180 in dry air (i.e., 21% oxygen and 79% nitrogen) with a source voltage of 2.0 V applied across the sensors. All sensors were measured with a source voltage of 2 V in dry (21% and oxygen 79%) and humid conditions (30, 60 and 90%). The working temperatures were regulated by varying the applied voltage while utilizing a thermocouple to record the correlating temperature at different voltages.

Mass flow controllers were used to vary the synthetic air and target gas concentrations in a gas cylinder mixture, while the variation in electrical resistance in the vicinity of target gas $R_g$ and air $R_a$ was measured by the Keithley 6487 picoammeter/ voltage source meter. The output measurements of all sensors were obtained in current (mA) and were further converted into resistance such that the response can be calculated. Since all the produced $In_2O_3$ sensors in this work are n-type material, the responses for all sensors were calculated using the $R_a/R_g$ formula.[36−38]

## 3. RESULTS AND DISCUSSION

**3.1. Structure and Microstructure Analysis.** The XRD patterns of the pure and $1Co-In_2O_3$, $1Ni-In_2O_3$, and $1Cu-$

$In_2O_3$ products are presented in Figure 3. The XRD diffraction patterns obtained from all $In_2O_3$ products demonstrated characteristics peaks matching very well with cubic bixbyite $In_2O_3$ (JCPDS Card no. 76−0152). No evidence of metallic and oxides of In, Co, Ni, and Cu elements was identified suggesting that all the transition metal dopant ions are successfully doped into the $In_2O_3$ lattice without altering the cubic bixbyite $In_2O_3$ structure. However, for the $1Co-In_2O_3$ product, a visible intensity increase of the diffraction peaks was noticed revealing high crystallinity, whereas $1Ni-In_2O_3$ and $1Cu-In_2O_3$ products revealed a decline in the intensity of the diffraction peaks, suggesting poor crystallinity. Figure 3(b) shows a magnified region of the most intense diffraction peak ascribed to the (222) plane in which a shift to lower $2\theta$ values was recognized for all doped products compared to the pure one. Such observations may be linked to the expansion of the $In_2O_3$ lattice due to ionic radius of $Ni^{2+}$ (0.63 Å), $Co^{2+}$ (0.72 Å), and $Cu^{2+}$ (0.72 Å) being smaller than the ionic radius of $In^{3+}$ (0.81 Å).[24,27,39] Furthermore, such shifting can be associated with lattice distortion induced by the addition of Co, Ni, and Cu ions into the $In_2O_3$ lattice.[40] The Debye− Scherrer formula[41,42] was applied to measure the average crystallite sizes for the pure, $1Co-In_2O_3$, $1Ni-In_2O_3$, and $1Cu-In_2O_3$ products in diameter using the (222) plane and
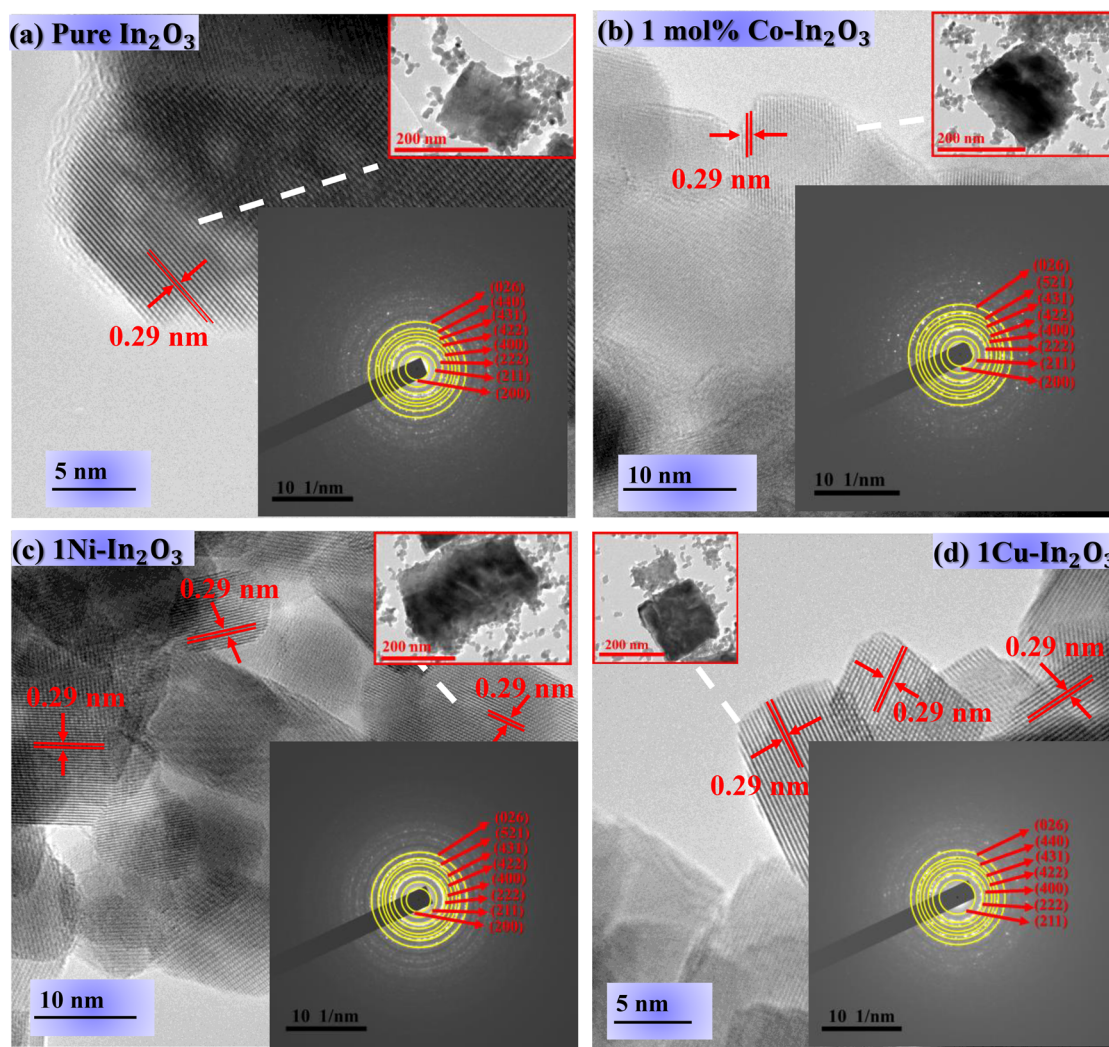
**Figure 4.** (a-d). HR-TEM images, the inset TEM images and the inset SAED of the pure, $1Co-In_2O_3$, $1Ni-In_2O_3$, and $1Cu-In_2O_3$ products.

were determined to be 30.9, 30.8, 30.6, and 30.6 nm, respectively. All doped $In_2O_3$ products revealed a slight reduction in crystallite sizes which suggests the generation of new nucleation centers by the dopant ions of the transitional metals.[43] Similar reduction in crystallites sizes were observed by Mhlongo et al.[44] for ZnO nanostructures doped with different transition metal ions. Moreover, a decrease in crystallite sizes can be explained by the lattice distortion of the host $In_2O_3$ induced by $Co^{2+}$, $Ni^{2+}$, and $Cu^{2+}$ ions which resulted in the decline in nucleation and the prevention of growth in the $In_2O_3$ nanoparticles.[45]

Figure 3(c-f) presents the SEM micrographs, average particle size, and EDS mapping of the pure and $1Co-In_2O_3$, $1Ni-In_2O_3$, and $1Cu-In_2O_3$ products. A cube-like morphology exhibiting 300 nm average edge length and consisting of interlinked nanoparticles was observed for the pure $In_2O_3$ product. However, this cube-like structure was found to be distorted into particle-like structure with addition of Co, Ni, Cu-dopant ions. Furthermore, the particle size distribution histograms demonstrated in the inset of Figure 3(c-f) showed inhomogeneous particle size distribution for all $In_2O_3$ products. The average particle sizes extracted by the ImageJ software were found to be 26, 25, 22, and 18 nm in diameter for the pure, $1Co-In_2O_3$, $1Ni-In_2O_3$, and $1Cu-In_2O_3$

products, demonstrating a decrease in particle sizes with the addition of different dopant ions. Such a trend can be associated with internal stresses or lattice distortion emerging from ionic radius mismatch between the transition metals and indium.[46] The electron dispersive spectroscopy (EDS) elemental maps in Figure 3(c) verified the uniform distribution of In and O for the pure $In_2O_3$ products, while the EDS map in Figure 3(d-f) showed the existence and distribution of Co, Ni, and Cu for $1Co-In_2O_3$, $1Ni-In_2O_3$, and $1Cu-In_2O_3$ products, respectively.

The TEM images for pure, $1Co-In_2O_3$, $1Ni-In_2O_3$, and $1Cu-In_2O_3$ products are presented in the inset of Figure 4(a-d). A cube-like morphology was observed for all TEM images of the produced $In_2O_3$ products, and this validates the morphology revealed by the SEM results. Therefore, all of the produced $In_2O_3$ products can be identified as nanocubes. However, it is apparent from these TEM images that the observed cube-like structures are assembled by nanoparticles interlinked to each other thus forming the cube-like morphology. Furthermore, the HR-TEM micrographs and insets of selected area electron diffraction (SAED) patterns of all $In_2O_3$ products are presented in Figure 4(a-d). The lattice fringes for all $In_2O_3$ products displayed an interplanar spacing of 0.29 nm belonging to the (222) plane of the bixbyite $In_2O_3$.
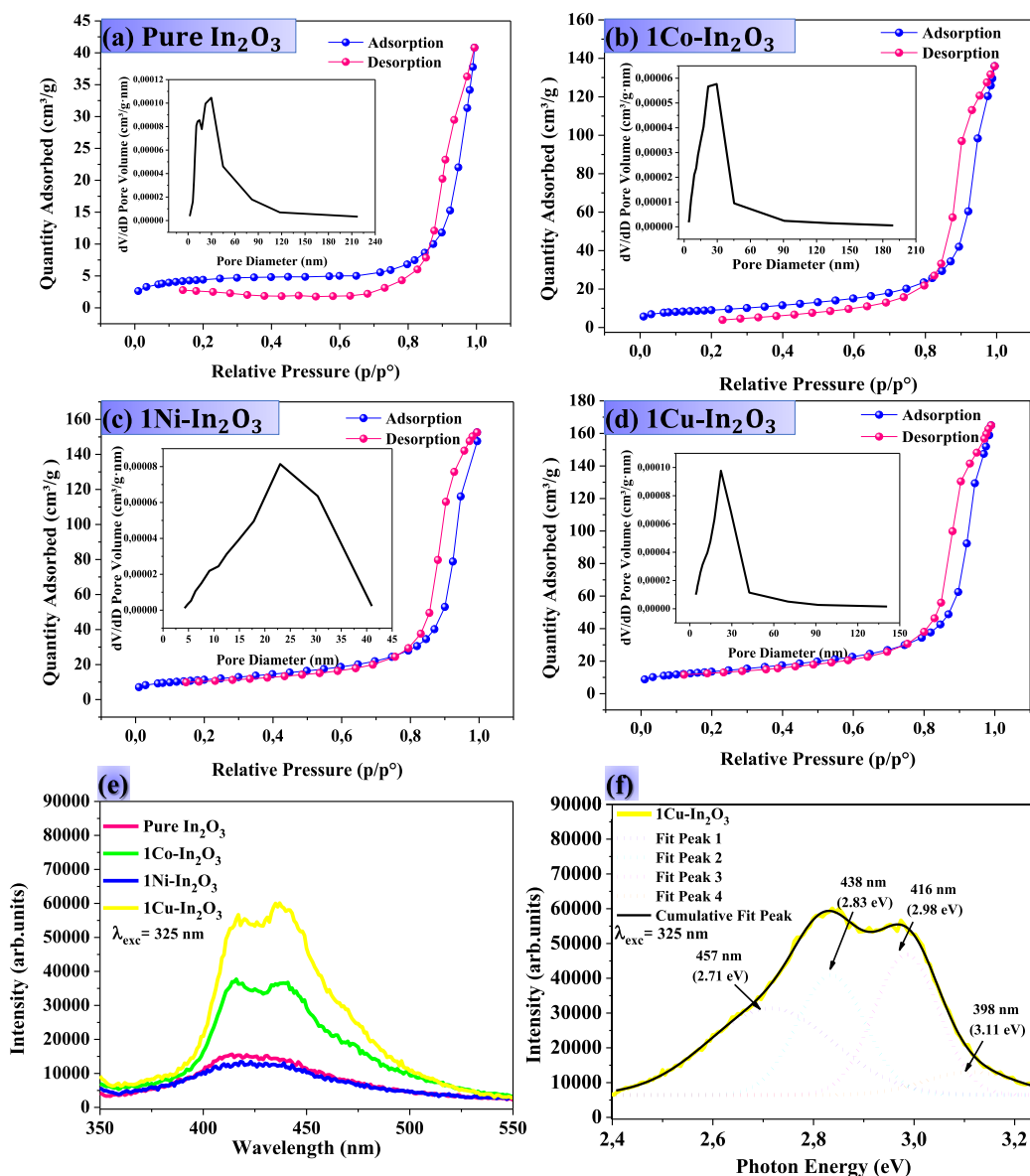
**Figure 5.** (a-d) Nitrogen adsorption/desorption isotherms and inset pore size distribution of (e) PL spectra of the pure, 1Co−In$_2$O$_3$, 1Ni−In$_2$O$_3$, and 1Cu−In$_2$O$_3$ products. (f) Fitted PL spectrum of 1Cu−In$_2$O$_3$ products.

All the diffraction rings for the corresponding SAED patterns of the pure, 1Co−In$_2$O$_3$, 1Ni−In$_2$O$_3$, and 1Cu−In$_2$O$_3$ products portrayed polycrystalline characteristic.

**3.2. Textural and Photoluminescence Analysis.** The high specific surface area of the SMOs is generally known to produce maximum active centers for target gas molecules to be adsorbed, while porosity enables inward and outward diffusion of the target gas molecules from the sensing film, thus enhancing the intrinsic gas sensing performance.[36,47−51] For this reason, the surface area and porous features for the pure, 1Co−In$_2$O$_3$, 1Ni−In$_2$O$_3$, and 1Cu−In$_2$O$_3$ products were examined via nitrogen adsorption/desorption tests, and the resulting isotherms and inserts depicting their pore size distribution are depicted in Figure 5(a-d). All In$_2$O$_3$ products displayed type-IV isotherms as per IUPAC categorization exhibiting a hysteresis loop at high pressures of $(0.8 < (P/P_0) > 1.0)$. This signifies the presence of mesopores having diameters within 2−50 nm range generated in between particles for all the produced In$_2$O$_3$ products.[46,47] To validate

the existence of mesopores, the BJH model analysis and adsorption isotherm (see inset Figure 5(a-d)) were investigated. The pore size distributions were found to be 27.0 for the pure, and 24.9, 23.6, 21.3 nm for the 1Co−In$_2$O$_3$, 1Ni−In$_2$O$_3$, 1Cu−In$_2$O$_3$ products, respectively, demonstrating mesoporous structure formation (2−50 nm) in all the In$_2$O$_3$ products. In accordance with adsorption/desorption isotherms, the pure, 1Co−In$_2$O$_3$, 1Ni−In$_2$O$_3$, and 1Cu−In$_2$O$_3$ products yielded a BET surface area of 14.3, 30.8, 39.6, and 47.0 m$^2$/g, respectively. Notably, the surface area increased with doping, and this correlates with the decrease in crystallite and particle size observed from XRD, SEM, and TEM results.

PL was adopted to evaluate the existence of structural defects in all of the produced In$_2$O$_3$ products. Figure 5(e) shows the PL emission spectra acquired from all In$_2$O$_3$ products after excitation at 325 nm. A strong broad blue emission band centered at 438 nm (2.83 eV) associated with deeper level emissions which are linked to oxygen vacancies ($Vo$) being present was apparent from all In$_2$O$_3$ products,[52]
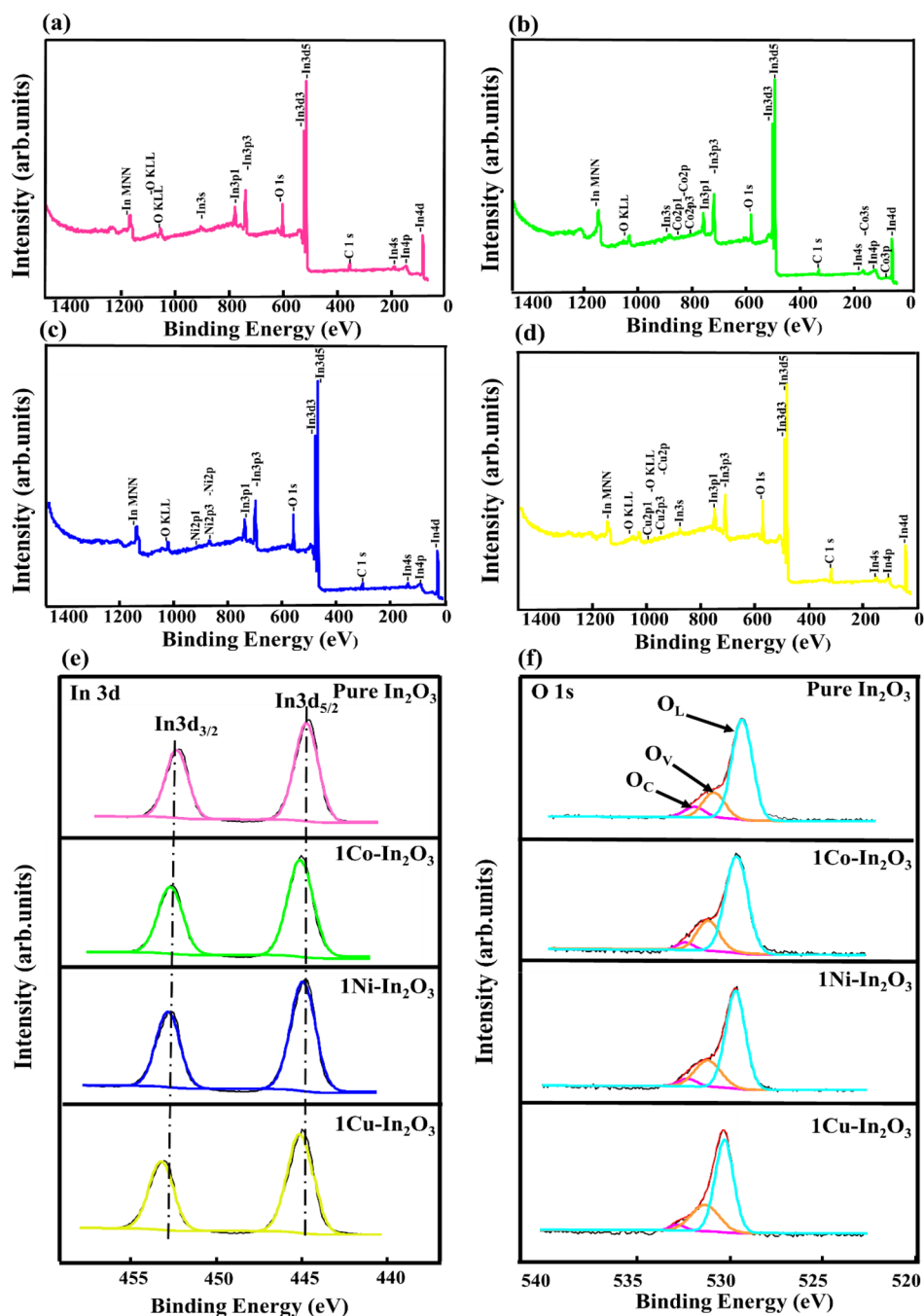
**Figure 6.** (a-d) full survey spectra for the pure and 1Co−In$_2$O$_3$, 1Ni−In$_2$O$_3$, and 1Cu−In$_2$O$_3$ products and high-resolution XPS spectra of the (e) In 3$d$ core-level (f) O 1$s$ core level for the pure and 1Co−In$_2$O$_3$, 1Ni−In$_2$O$_3$, and 1Cu−In$_2$O$_3$ products.

together with a weak shoulder emission peak in the ultraviolet region at 398 nm (3.11 eV) which can be associated with near band emission.[53] The 1Cu−In$_2$O$_3$ product displayed the most intense emission band which is an indication of a high concentration of *Vo* defects being present. The PL emission spectrum of the 1Cu−In$_2$O$_3$ product was then fitted with several Gaussian functions to identify the contributing defects as shown in Figure 5(f). The emission peak centered at 3.11 eV can be linked with distinctive near-band emission (NBE).[54] Emission peaks at 2.71, 2.83, and 2.98 eV can be associated with deeper level emissions.[55−59]

**3.3. XPS Analysis.** XPS analysis was conducted to investigate the chemical states of elements present on the

surface of all of the In$_2$O$_3$ products. Figure 6(a-d) presents the full XPS survey spectra for the pure and 1Co−In$_2$O$_3$, 1Ni−In$_2$O$_3$, and 1Cu−In$_2$O$_3$ products in which the coexistence of In, Co, Ni, Cu, and C are displayed. The high-resolution XPS spectra for all In$_2$O$_3$ products corresponding to the In 3$d$ core-level characterized by spin−orbit doublets of In 3$d_{5/2}$ and In 3$d_{3/2}$ situated at 444.12−444.47 and 451.69−452.03 eV, respectively, are displayed in Figure 6(e). This demonstrates that In ions exist in the In$^{3+}$ oxidation state.[60] The high-resolution XPS spectra correlating to the O 1$s$ core-level spectra of all of the In$_2$O$_3$ products are presented in Figure 6(f). The O 1$s$ core-level spectrum was fitted into three fitted peaks for each sample using the Gaussian function, and the

components can be attributed to the lattice oxygen ($O_L$), the oxygen vacancies ($O_V$), and the chemisorbed oxygen species ($O_C$) situated at 529.5, 531.3, and 532.5 eV, respectively.[61] The relative intensities of the $O_L$, $O_V$, and $O_C$ for all the $In_2O_3$ products are displayed in Table 1. It was realized that upon

**Table 1. Intensity of the O 1$s$ Gaussian Fits of the Pure $In_2O_3$, 1Co−$In_2O_3$, 1Ni−$In_2O_3$, and 1Cu−$In_2O_3$**

| sample | $O_L$ area (%) | $O_C$ area (%) | $O_V$ area (%) | $O_V/O_L$ area (%) |
|--------|------|------|------|------|
| pure | 72.85 | 7.67 | 19.48 | 0.26 |
| 1Co−$In_2O_3$ | 73.75 | 4.45 | 21.81 | 0.29 |
| 1Ni−$In_2O_3$ | 70.21 | 4.98 | 24.81 | 0.35 |
| 1Cu−$In_2O_3$ | 67.46 | 3.60 | 28.94 | 0.42 |

introduction of the dopant ions, the intensity and percentage area value of the $O_V$ component increased. In comparison to other $In_2O_3$ products, the 1Cu−$In_2O_3$ product presented the highest relative intensity and percentage area value of the $O_V$ component. The higher $O_V$ component suggests a larger concentration of $O_V$ which can assist in oxygen ions to be adsorbed on the surface of the $In_2O_3$ sensor material with Cu addition, thus promoting more reactive sites for the target gas to be adsorbed and desorbed. Due to the low dopant amount of the Co, Ni, Cu inside $In_2O_3$, high-resolution spectra for the Co 2$p$, Ni 2$p$, and Cu 2$p$ core level could not be fitted.

**3.4. Gas Sensing Performance.** Figure 7(a) displays the resistance in air of the pure and 1Co−$In_2O_3$, 1Ni−$In_2O_3$, and 1Cu−$In_2O_3$ sensors. The 1Ni−$In_2O_3$ and 1Cu−$In_2O_3$ sensors portrayed a decrease in resistance with rising working temperature from 40 to 160 °C. This observation can be
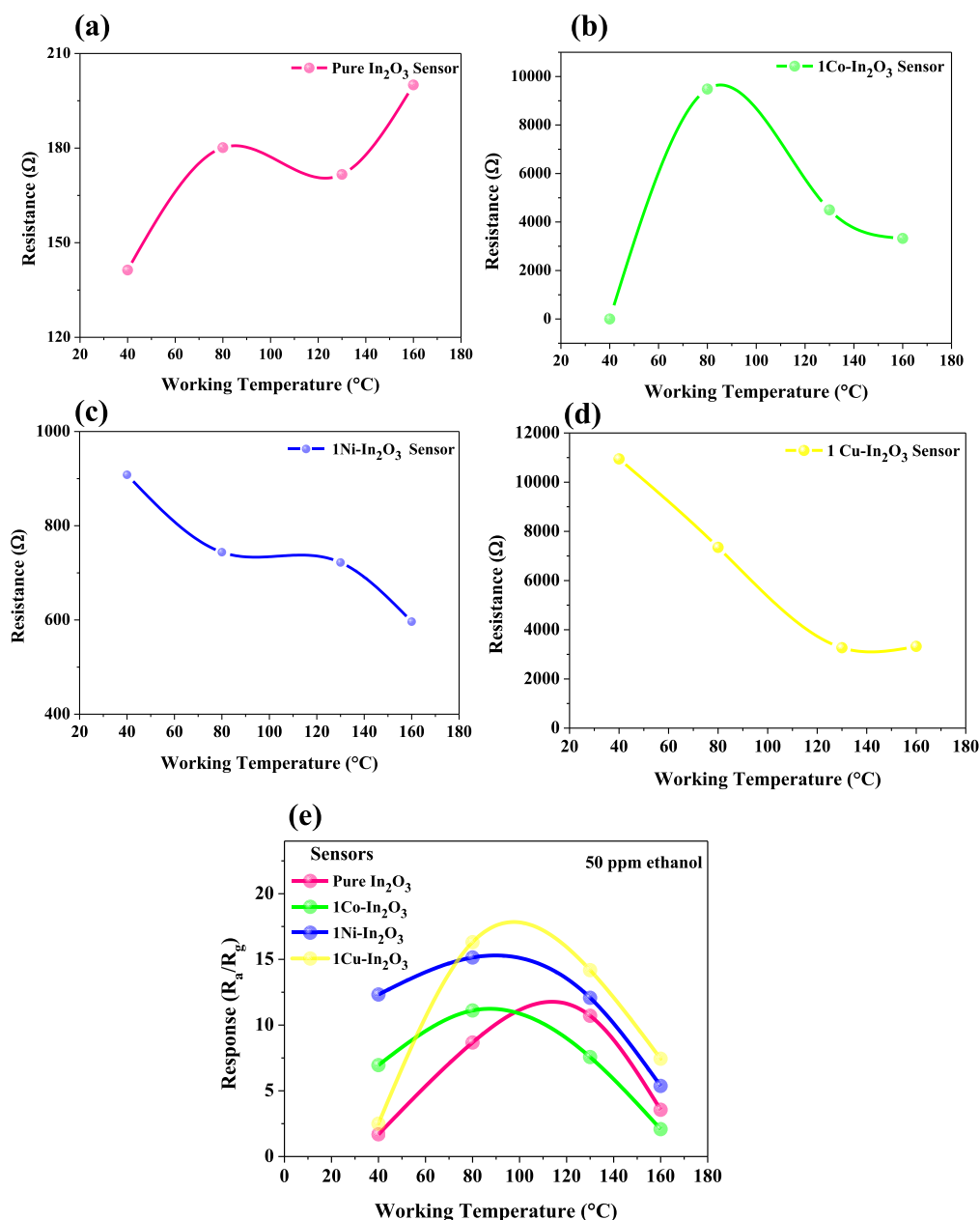


**Figure 7.** (a-d) Resistance in air, (e) responses of the pure, 1Co−$In_2O_3$, 1Ni−$In_2O_3$, and 1Cu−$In_2O_3$ based sensors as a function of the working temperature from 40 to 160 °C toward 50 ppm ethanol.
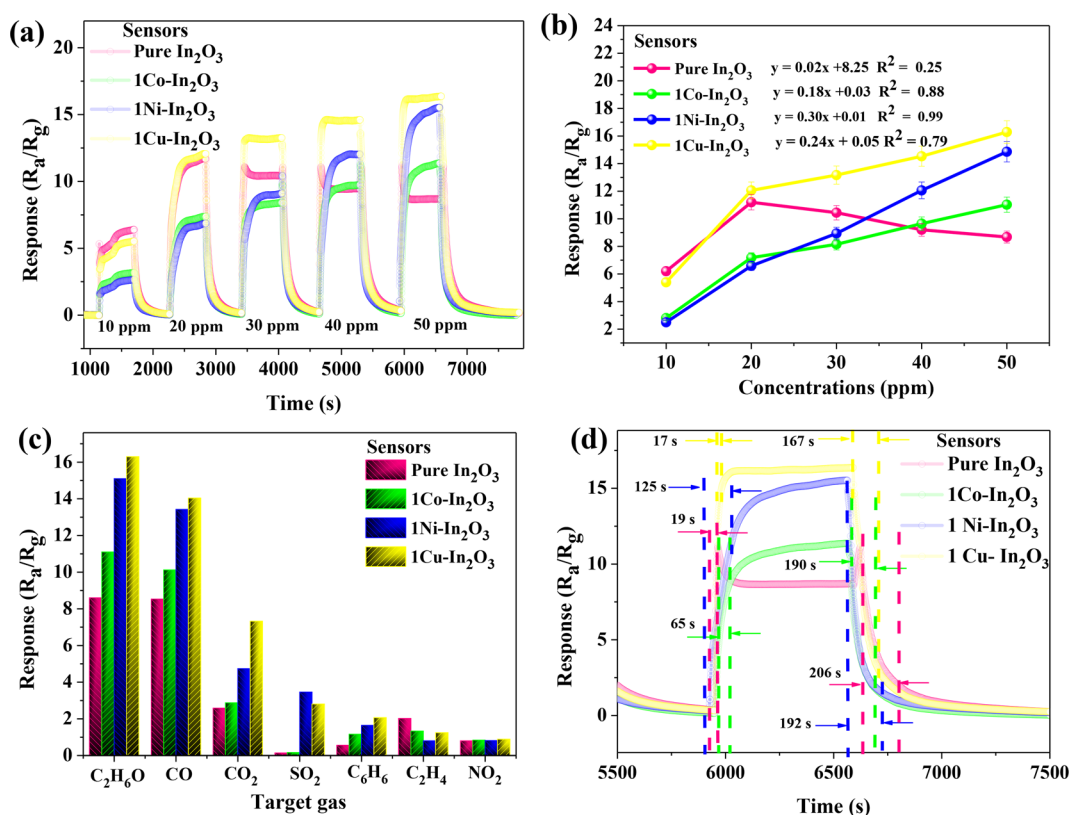
**Figure 8.** (a)-(b) Response curves versus different ethanol concentration, (c) comparison of responses toward 50 ppm of different gases, (d) response/recovery times of the pure, 1Co−In$_2$O$_3$, 1Ni−In$_2$O$_3$, and 1Cu−In$_2$O$_3$ based sensors toward 50 ppm of ethanol gas at 80 °C.

explained as follows: as the working temperature rises the thermal excitation is induced, which enables additional electrons to be excited to the conduction band.[48,62] Meanwhile, the 1Co−In$_2$O$_3$ sensor displayed an increase in resistance at low working temperatures ranging from 40 to 80 °C and thereafter a decline in resistance from 80 to 160 °C. The high resistance at lower working temperatures can be explained by adsorbed oxygen ions capturing electrons from the conduction band of the 1Co−In$_2$O$_3$ sensor material resulting in the electron carrier concentrations being reduced, while the decrease in resistance at higher working temperatures can be associated with an increase in electron carrier concentrations resulting from excitation of more carriers at higher working temperatures.[63,64] The pure In$_2$O$_3$ sensor presented increasing resistance with a rising working temperature (40−160 °C). The observed trend can be ascribed to more electrons being trapped from the conduction band by the adsorbed oxygen ions as the working temperature rises thus leading to the electron depletion layer and the Schottky barrier to be produced.[60,63]

Figure 7(e) presents the responses of the pure and 1Co−In$_2$O$_3$, 1Ni−In$_2$O$_3$, 1Cu−In$_2$O$_3$ sensors subjected to different working temperatures toward 50 ppm of ethanol vapor. The sensor based on pure In$_2$O$_3$ presented optimum response at 130 °C, while those based on 1Co−In$_2$O$_3$, 1Ni−In$_2$O$_3$, and 1Cu−In$_2$O$_3$ yielded maximum response at 80 °C. The obtained low response values at low working temperatures can be explained by the ethanol vapor molecules having inadequate thermal energy to participate in the reaction with adsorbed oxygen ions.[61], Meanwhile, the observed drop in response at high working temperatures beyond sensors optimal working temperatures of 130 and 80 °C for pure and 1Co−

In$_2$O$_3$, 1Ni−In$_2$O$_3$, and 1Cu−In$_2$O$_3$ sensors may be linked to the prevalence of the desorption process which restricts the ethanol vapor molecules to be adsorbed, as well as usage of the In$_2$O$_3$ sensing layer.[20] Based on the temperature dependence investigations, all sensing tests were performed at 130 °C for the pure and 80 °C for 1Co−In$_2$O$_3$, 1Ni−In$_2$O$_3$, and 1Cu−In$_2$O$_3$ sensors.

Figure 8(a) shows transient response curves of the pure, 1Co−In$_2$O$_3$, 1Ni−In$_2$O$_3$, and 1Cu−In$_2$O$_3$ sensors toward ethanol from 10 to 50 ppm at 80 °C. As anticipated, all sensors displayed a rapid increase upon exposure to each concentration of ethanol until reaching a saturation value before dropping to the baseline upon removal of ethanol vapor from the system. This response behavior shows a competent reversibility attribute of the sensors and demonstrates that all sensors are n-type semiconductors with electrons as majority charge carriers. In contrast to other sensors, the Cu-doped In$_2$O$_3$ based sensor displayed a greater response value of 15.3 at 50 ppm of ethanol vapor. The reason for this improved response for the 1Cu−In$_2$O$_3$ sensor can be related to the 3D cube-like structure which comprised the largest surface area and porous structure which aided in ethanol gas diffusion.[20] To further authenticate the dependence of the sensors response on the different ethanol concentrations, the response curves of all sensors against varying target gas concentrations were fitted, and the results are presented in Figure 8(b). All doped In$_2$O$_3$ sensors displayed a rise in response with an increase in ethanol concentrations. This can be explained by the surface reaction between the ethanol gas molecules and adsorbed oxygen molecules which depends on the high surface coverage of the ethanol gas.[62] Meanwhile, the observed decline in response with rising ethanol concentrations for pure In$_2$O$_3$ sensor can be
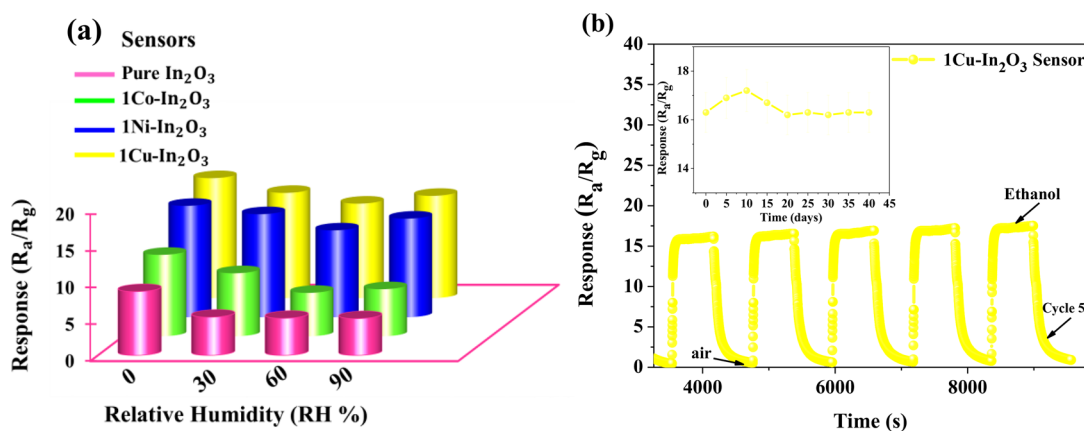
**Figure 9.** (a) Responses to different relative humidity conditions for the pure and 1Co$-$In$_2$O$_3$, 1Ni$-$In$_2$O$_3$, and 1Cu$-$In$_2$O$_3$ sensors toward 50 ppm of ethanol gas at 80 °C. (b) Reproducibility plot with the inset of stability measurements at 80 °C toward 50 ppm of ethanol gas for the 1Cu$-$In$_2$O$_3$ sensor.

attributed to surface reactions between adsorbed oxygen molecules and ethanol gas molecules reaching saturation.[44] Furthermore, the gradient of the response curves Figure 8(b) shows the sensitivities of all sensors, known as the capabilities of a sensor to distinguish small concentration changes of the analyte gas.[48,65] Therefore, the sensitivity values were obtained to be 0.02 for the pure In$_2$O$_3$ sensor and 0.18, 0.30, and 0.24 for 1Co$-$In$_2$O$_3$, 1Ni$-$In$_2$O$_3$, and 1Cu$-$In$_2$O$_3$ sensors, respectively. It is apparent that 1Ni$-$In$_2$O$_3$ and 1Cu$-$In$_2$O$_3$ sensors exhibited the largest sensitivity values, and this shows that both sensors have the competence to display the maximum response, and this is favorable to monitoring ethanol vapor at low concentrations. On this basis, the limit of detection (LOD) was obtained via using the following formula:[48]

$$LOD = 3\left(\frac{noise_{rms}}{slope}\right) \tag{1}$$

The LOD was calculated to be 4.12, 1.76, 1.44, and 1.50 ppm for the pure, 1Co$-$In$_2$O$_3$, 1Ni$-$In$_2$O$_3$, and 1Cu- In$_2$O$_3$ sensors, respectively.

As displayed in Figure 8(c), selectivity was also evaluated by exposing all sensors to 50 ppm of different gases, including ethanol (C$_2$H$_6$O), carbon monoxide (CO), ethylene (C$_2$H$_4$), sulfur dioxide (SO$_2$), benzene (C$_6$H$_6$), nitrogen dioxide (NO$_2$), and carbon dioxide (CO$_2$), at 80 °C (all doped In$_2$O$_3$ sensors) and 130 °C (pure In$_2$O$_3$ sensor). All sensors exhibited a maximum response toward ethanol in comparison to other gases. This can be explained by the value of lowest unoccupied molecular orbit (LUMO) energy and the low binding energy of the ethanol vapor in comparison to other gases.[19,65−67] This makes the ethanol easier to break down and partake in the sensing reaction on the sensor material surface by transferring electrons into the conduction band. Another reason can be linked to other gases having different optimal working temperatures, therefore at 80 °C some gases may likely not have been adsorbed on the In$_2$O$_3$ cube-like sensor material due to insufficient energies.[48,65] Moreover, at 80 °C, ethanol molecules may have been more chemically reactive with the adsorbed oxygen species on the surface of the sensor material in contrast to other gases, thereby resulting in more electrons to be released into the conduction band of the cube-

like In$_2$O$_3$ product and hence the observed high selectivity toward ethanol.[49]

The response and recovery times of all sensors were examined, and the results are shown in Figure 8(d). The pure, 1Co$-$In$_2$O$_3$, 1Ni$-$In$_2$O$_3$, and 1Cu$-$In$_2$O$_3$ sensors presented response/recovery times of 19/206, 65/190, 125/192, and 17/167s, respectively. Evidently, the 1Cu$-$In$_2$O$_3$ sensor presented rapid response/recovery times in contrast to its counterparts which can be attributed to the fast rate of adsorption/desorption of ethanol gas molecules occurring on the sensor material. On the other hand, the large reactive centers produced by the elevated specific surface, as well as diffusion generated by the porous feature of the 1Cu$-$In$_2$O$_3$ cube-like product can be associated with the improved response/recovery times.[49]

Considering that water vapor is a significant parameter that can determine the full sensing capability and commercial usage of the gas sensor, the ethanol gas sensing performance of all sensors in various humidity environments was examined, and the plots are portrayed in Figure 9(a). All sensors exhibited a declining trend in response as the humidity environment was elevated from 0 to 90%. The reason for this observed trend can be ascribed to minimal interaction occurring between the ethanol vapor molecules and the In$_2$O$_3$ cube-like sensing material, arising from the adsorption of additional water molecules on the sensor material as the humidity is increased.[19,27,67] This will result in adsorption of the ethanol vapor molecules on the sensing material to be weakened, hence the observed drop in response. Notably, the 1Cu$-$In$_2$O$_3$ sensor still exhibited the highest response at various humidity levels among other sensors. In particular, the 1Cu$-$In$_2$O$_3$ sensor maintained 85.2% of its response value as the humidity improved to 90%, which is an indication of its capability to be utilized for ethanol detection under environments, thus making it feasible for commercial applications particularly in the food sector. The response/recovery curves for the 1Cu$-$In$_2$O$_3$ sensor are shown in Figure 9(b) to evaluate the reproducibility of the recorded response signal under identical sensing conditions. As displayed in Figure 9(b), a similar response signal over 5 cycles toward 50 ppm ethanol at 80 °C was produced suggesting good reproducibility. While the inset in Figure 9(b) portrays the long-term stability of the 1Cu$-$In$_2$O$_3$ sensor evaluated over 40 days at 5 day intervals toward 50 ppm of ethanol at 80 °C. A steady response with minimal changes

was maintained, demonstrating good stability of the 1Cu–In$_2$O$_3$ sensor.

A contrast of the gas sensing characteristics of ethanol sensors based on nanostructured In$_2$O$_3$ products doped with different metal ions and 1Cu–In$_2$O$_3$ sensor are presented in Table 2. The 1Cu–In$_2$O$_3$ sensor exhibited excellent gas sensing results that could be used to detect ethanol at relatively low working temperatures and at low ethanol levels.

**Table 2. Comparison of Ethanol Sensing Properties of 1Cu–In$_2$O$_3$ Sensor to Other In$_2$O$_3$ Based Sensors on Different Metal Ion Dopants**

| sensing material and morphology | T (°C) | conc. (ppm) | response | $\tau_{res}/\tau_{rec}$ (s) | ref |
|---|---|---|---|---|---|
| Co-doped In$_2$O$_3$ nanowires | 300 | 100 | 16.5 | 2/3 | 68 |
| Ni-doped In$_2$O$_3$ nanotubes | 220 | 100 | 49.74 | 3/49 | 24 |
| Co-doped In$_2$O$_3$ nanocylinder | 210 | 100 | 14.6 | 21/107 | 26 |
| Cu-doped In$_2$O$_3$ nanofibers | 250 | 100 | 3 | - | 27 |
| Mn-doped In$_2$O$_3$ nanoparticles | 300 | 100 | 23 | 32/49 | 55 |
| Er-doped In$_2$O$_3$ nanoribbons | 220 | 100 | 4.8 | 12/13 | 69 |
| Pb-doped In$_2$O$_3$ nanostructures | 250 | 100 | 32.6 | 2.2/0.7 | 70 |
| Au-doped In$_2$O$_3$ nanoparticles | 200 | 100 | 106 | - | 71 |
| Ce-doped In$_2$O$_3$ nanospheres | 330 | 100 | 146 | 14/40 | 72 |
| 1Cu–In$_2$O$_3$ sensor | 80 | 50 | 15.3 | 17/167 | This work |

### 3.5. Sensing Mechanism for 1Cu–In$_2$O$_3$ Based Sensor.

The gas sensing mechanism of 1Cu–In$_2$O$_3$ sensor can be inferred from resistance variation occurring in the presence of air and ethanol vapor molecules. The fluctuation in resistance depends on the SMO's density charge carrier. Since the 1Cu–In$_2$O$_3$ sensor is an n-type SMO, then the density charge carriers are electrons.[73] Therefore, when the 1Cu–In$_2$O$_3$ sensor is exposed to ambient air as illustrated in Figure 10(a), the oxygen molecules will adsorb on its surface and generate chemisorbed oxygen ions by apprehending electrons from the conduction band of the 1Cu–In$_2$O$_3$ product.[74,75] The type of chemisorbed oxygen ions forming on the surface relies on the working temperature (O$_2^-$, T < 100 °C; O$^-$, 100 ≤ T ≤ 300 °C; O$^{2-}$, T > 300 °C)[76−77,78,79] In this study, the optimal working temperature obtained for this sensor is 80 °C, therefore O$_2^-$ is predominantly adsorbed on the 1Cu–In$_2$O$_3$ sensor material as per equation 1. The formed O$_2^-$ ions result in the formation of a thick electron depletion layer (EDL) on the sensor material; therefore, a high resistance will be produced by the 1Cu–In$_2$O$_3$ sensor.[80]

$$O_{2(ads)} + e^- \rightarrow O_2^- \tag{2}$$

Conversely, when the 1Cu–In$_2$O$_3$ sensor is introduced to ethanol as illustrated in Figure 10(b), the ethanol vapor molecules will adsorb on its surface and chemically react with the $O_2^-$ molecules and release the apprehended electrons into the In$_2$O$_3$ conduction band as per eq 2 below.[81]

$$CH_3CH_2OH_{(ads)} + 6O_{2(ads)}^-$$
$$\rightarrow 2CO_{2(ads)} + 3H_2O_{(ads)} + 6e^- \tag{3}$$
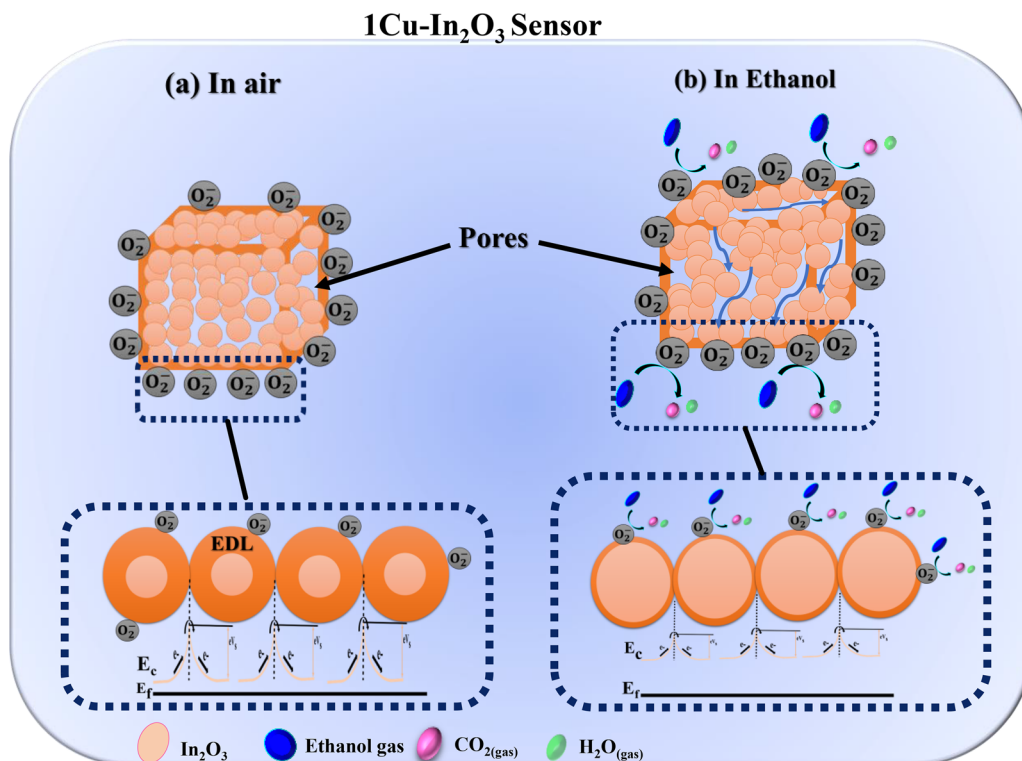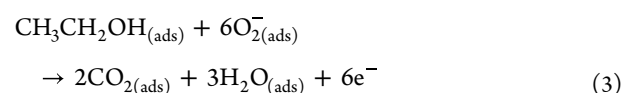


**Figure 10.** Gas sensing mechanism of 1Cu–In$_2$O$_3$ sensor in the presence of (a) air and (b) ethanol target gas.

As electrons are being released into the conduction band, a thin EDL will be created, which leads to the observed reduction in the resistance of the $1Cu-In_2O_3$ sensor.

The obtained improved ethanol gas sensing properties of the $1Cu-In_2O_3$ sensor can therefore be explained by several reasons including surface area, morphology, and surface defects. As demonstrated by the XRD, SEM, and TEM analysis, $1Cu-In_2O_3$ products presented small-scale average crystallite size and particle size in diameter, which led to the largest specific surface area. In gas sensing, maximum specific surface area has been proven to endow a high number active sites adsorption of oxygen and ethanol molecules thus leading to improved gas sensor response. Also, the interconnected particles forming the cube-like structure as observed from TEM and the mesoporous feature contributes to efficient diffusion of ethanol molecules, allowing improved contact between the $In_2O_3$ sensing material and the ethanol vapor molecules. The PL analysis showed that $1Cu-In_2O_3$ products consist of high content of oxygen defects among its counterparts. The presence of $V_O$ in high concentrations will provide more oxygen molecules to be adsorbed, thereby increasing the gas response.[82,83] XPS analysis showed that the $1Cu-In_2O_3$ product has the highest relative intensity and percentage area value of the $O_V$ component indicating higher content of oxygen vacancies in comparison to other $In_2O_3$ products. The existence of these oxygen vacancies in large amounts provides oxygen adsorption on the sensor layer and provides more interaction between the ethanol and $In_2O_3$, hence the produced high response to detection of ethanol.

## 4. CONCLUSIONS

In summary, pure $1Co-In_2O_3$, $1Ni-In_2O_3$, and $1Cu-In_2O_3$ products were synthesized via a hydrothermal approach. Results related to XRD showed that all of the $In_2O_3$ products exhibited a bixbyite cubic symmetry. Among other $In_2O_3$ products, the $1Cu-In_2O_3$ product displayed the smallest crystallite and particle sizes as confirmed by the XRD, SEM, and TEM findings. PL and XPS analyses demonstrated the existence of oxygen vacancies in large amounts for the $1Cu-In_2O_3$ product in comparison to other $In_2O_3$ products. The BET results showed that the mesoporous feature of the $1Cu-In_2O_3$ product displayed the highest specific surface area of 47.0 $m^2/g$. Furthermore, the gas sensing test measurements revealed maximum response, high selectivity, and improved response/recovery times toward ethanol gas at 80 °C from the Cu ion doped $In_2O_3$ sensor in contrast to other sensors. These enhanced gas sensing characteristics were associated with the porous feature and the maximum specific surface area which endowed efficient ethanol gas diffusion and large active sites for ethanol vapor molecule adsorption. Therefore, the Cu-doped $In_2O_3$ sensor at 1 mol % serves as a new approach to engineer mesoporous attributes and large surface area on a 3D cube-like $In_2O_3$ product to achieve improved ethanol responsivity, which can be used for monitoring ethanol at minimal the working temperature and concentrations.

## AUTHOR INFORMATION

**Corresponding Author**

Gugu H. Mhlongo − *Centre for Nanostructures and Advanced Materials (CeNAM), DSI-CSIR Nanotechnology Innovation Centre, Council for Scientific and Industrial Research, Pretoria 0001, South Africa; Department of Physics, University of the Free State, Bloemfontein ZA9300, South Africa;* orcid.org/0000-0002-7888-1069; Email: gmhlongo@csir.co.za

**Authors**

Mosima B. Kgomo − *Centre for Nanostructures and Advanced Materials (CeNAM), DSI-CSIR Nanotechnology Innovation Centre, Council for Scientific and Industrial Research, Pretoria 0001, South Africa; Department of Physics, University of the Free State, Bloemfontein ZA9300, South Africa*

Hendrik C. Swart − *Department of Physics, University of the Free State, Bloemfontein ZA9300, South Africa;* orcid.org/0000-0001-5233-0130

Complete contact information is available at:
https://pubs.acs.org/10.1021/acsomega.3c04453

**Notes**

The authors declare no competing financial interest.

## REFERENCES

(1) Ghasemi, F.; Ghasemi, M.; Eftekhari, L.; Soleimanian, V. Comparison and influence of metal dopants on the opto-electrical, microstructure and gas sensing properties of nanostructured indium oxide films,. *Opt. Laser Technol.* **2022**, *146*, 107564.

(2) Chen, X.; et al. Preparation of Fe-doped $In_2O_3$ gas sensing semiconductor by one-step impregnation with enhanced ethanol sensing,. *Chem. Phys. Lett.* **2019**, *722*, 96−103.

(3) Zhang, Z.-G.; Wang, X.-X.; Zhang, J.; Yu, M.; Zhang, J.-C.; Zhang, H.-D.; Long, Y.-Z. Recent advances in 1D micro- and nanoscale indium oxide structures,. *J. Alloys Compd.* **2018**, *752*, 359−375.

(4) Hu, X.; et al. Highly enhanced $NO_2$ sensing performances of Cu-doped $In_2O_3$ hierarchical flowers,. *Sensors Actuators B Chem.* **2015**, *221*, 297−304.

(5) Pawar, K. K.; et al. Fabrication of enhanced sensitive and selective porous indium oxide nanocube sensor for $NO_2$ detection,. *Ceram. Int.* **2021**, *47* (2), 2430−2440.

(6) Tamaki, J.; Naruo, C.; Yamamoto, Y.; Matsuoka, M. Sensing properties to dilute chlorine gas of indium oxide based thin film sensors prepared by electron beam evaporation,. *Sensors and Actuators, B: Chemical* **2002**, *83* (1−3), 190−194.

(7) Dong, H.; et al. Hierarchically rosette-like $In_2O_3$ microspheres for volatile organic compounds gas sensors,. *Sensors Actuators, B Chem.* **2013**, *178*, 302−309.

(8) Nguyen, T. T. D.; Choi, H. N.; Ahemad, M. J.; Van Dao, D.; Lee, I. H.; Yu, Y. T. Hydrothermal synthesis of $In_2O_3$ nanocubes for highly responsive and selective ethanol gas sensing,. *J. Alloys Compd.* **2020**, *820*, 153133.

(9) Zachut, M.; Shapiro, F.; Silanikove, N. Detecting ethanol and acetaldehyde by simple and ultrasensitive fluorimetric methods in compound foods,. *Food Chem.* **2016**, *201*, 270−274.

(10) Wen, G.; Li, Z.; Choi, M. M. F. Detection of ethanol in food: A new biosensor based on bacteria,. *J. Food Eng.* **2013**, *118* (1), 56−61.

(11) Liu, K.; Zhang, C. Volatile organic compounds gas sensor based on quartz crystal microbalance for fruit freshness detection: A review,. *Food Chem.* **2021**, *334*, 127615.

(12) Lavilla, T.; Recasens, I.; López, M. L. Production of volatile aromatic compounds in Big Top nectarines and Royal Glory peaches

during maturity,. *IV International Conference on Postharvest Science* **2000**, *553*, 233−234, DOI: 10.17660/ActaHortic.2001.553.51.

(13) Beltrán, G.; Bejaoui, M. A.; Jimenez, A.; Sanchez-Ortiz, A. Ethanol in olive fruit. Changes during ripening,. *J. Agric. Food Chem.* **2015**, *63* (22), 5309−5312.

(14) Nair, S.; Cope, K.; Terence, R. H.; Diehl, A. M. Obesity and female gender increase breath ethanol concentration: potential implications for the pathogenesis of nonalcoholic steatohepatitis,. *Am. J. Gastroenterol.* **2001**, *96* (4), 1200−1204.

(15) Hu, Z.-D.; et al. Cobalt monosulfide nanofibers: ethanol sensing and magnetic properties,. *Rare Met.* **2021**, *40*, 1554−1560.

(16) Gai, L.-Y.; et al. Recent advances in ethanol gas sensors based on metal oxide semiconductor heterojunctions,. *Rare Met.* **2022**, *41* (6), 1818−1842.

(17) Mirzaei, A.; Leonardi, S. G.; Neri, G. Detection of hazardous volatile organic compounds (VOCs) by metal oxide nanostructures-based gas sensors: A review,. *Ceram. Int.* **2016**, *42* (14), 15119−15141.

(18) Zhang, Y.; et al. The role of Ce doping in enhancing sensing performance of ZnO-based gas sensor by adjusting the proportion of oxygen species,. *Sensors Actuators. B Chem.* **2018**, *273*, 991−998.

(19) Zhang, S.; Lin, T.; Song, P.; Sun, J.; Wang, Q. MOF-derived $In_2O_3$ nanotubes/$Cr_2O_3$ nanoparticles composites for superior ethanol gas-sensing performance at room temperature,. *Ceram. Int.* **2022**, *48*, 28334.

(20) Song, P.; Han, D.; Zhang, H.; Li, J.; Yang, Z.; Wang, Q. Hydrothermal synthesis of porous $In_2O_3$ nanospheres with superior ethanol sensing properties,. *Sensors actuators B Chem.* **2014**, *196*, 434−439.

(21) Zhang, S.; Song, P.; Yan, H.; Yang, Z.; Wang, Q. A simple large-scale synthesis of mesoporous $In_2O_3$ for gas sensing applications,. *Appl. Surf. Sci.* **2016**, *378*, 443−450.

(22) Elouali, S.; Bloor, L. G.; Binions, R.; Parkin, I. P.; Carmalt, C. J.; Darr, J. A. Gas sensing with nano-indium oxides ($In_2O_3$) prepared via continuous hydrothermal flow synthesis,. *Langmuir* **2012**, *28* (3), 1879−1885.

(23) Sun, X.; Hao, H.; Ji, H.; Li, X.; Cai, S.; Zheng, C. Nanocasting synthesis of $In_2O_3$ with appropriate mesostructured ordering and enhanced gas-sensing property,. *ACS Appl. Mater. Interfaces* **2014**, *6* (1), 401−409.

(24) Bai, J.; et al. Role of nickel dopant on gas response and selectivity of electrospun indium oxide nanotubes,. *J. Colloid Interface Sci.* **2020**, *560*, 447−457.

(25) Zhang, Y.; Cao, J.; Wang, Y. Ultrahigh methane sensing properties based on Ni-doped hierarchical porous $In_2O_3$ microspheres at low temperature,. *Vacuum* **2022**, *202*, 111149.

(26) Yong, P.; Wang, S.; Zhang, X.; Pan, H.; Shen, S. MOFs-derived Co-doped $In_2O_3$ hollow hexagonal cylinder for selective detection of ethanol,. *Chem. Phys. Lett.* **2022**, *795*, 139517.

(27) Zhang, Y.; et al. Electrospun Cu-doped $In_2O_3$ hollow nanofibers with enhanced $H_2S$ gas sensing performance,. *J. Adv. Ceram.* **2022**, *11* (3), 427−442.

(28) Sun, Y.; et al. Synthesis of $In_2O_3$ nanocubes, nanocube clusters, and nanocubes-embedded Au nanoparticles for conductometric CO sensors,. *Sensors Actuators B Chem.* **2021**, *345*, 130433.

(29) Zhang, S.; et al. An acetone gas sensor based on nanosized Pt-loaded $Fe_2O_3$ nanocubes,. *Sensors Actuators B Chem.* **2019**, *290*, 59−67.

(30) Bai, L.; et al. Design of Ag-decorated ZnO concave nanocubes using ZIF-8 with dual functional catalytic ability for decoloring dyes,. *CrystEngComm* **2018**, *20* (21), 2980−2988.

(31) Zhai, J.; Kang, Q.; Liu, Q.; Lai, D.; Lu, Q.; Gao, F. In-situ generation of $In_2O_3$ nanoparticles inside $In[Co(CN)_6]$ quasi-metal-organic-framework nanocubes for efficient electroreduction of $CO_2$ to formate,. *J. Colloid Interface Sci.* **2022**, *608*, 1942−1950.

(32) Tian, Z.; Song, P.; Yang, Z.; Wang, Q. Reduced graphene oxide-porous $In_2O_3$ nanocubes hybrid nanocomposites for room-temperature NH3 sensing,. *Chin. Chem. Lett.* **2020**, *31* (8), 2067−2070.

(33) Shanmugasundaram, A.; Ramireddy, B.; Basak, P.; Manorama, S. V.; Srinath, S. Hierarchical In $(OH)_3$ as a precursor to mesoporous $In_2O_3$ nanocubes: a facile synthesis route, mechanism of self-assembly, and enhanced sensing response toward hydrogen,. *J. Phys. Chem. C* **2014**, *118* (13), 6909−6921.

(34) Lu, Y.; et al. MOF-templated synthesis of porous $Co_3O_4$ concave nanocubes with high specific surface area and their gas sensing properties,. *ACS Appl. Mater. Interfaces* **2014**, *6* (6), 4186−4195.

(35) Van Minh Hai, H.; Cuong, N. D.; Mai, H. D.; Long, H. T.; Phuong, T. Q.; Dang, T. K.; Thong, L. V.; Viet, N. N.; Van Hieu, N. Superior detection and classification of ethanol and acetone using 3D ultra-porous $\gamma$-$Fe_2O_3$ nanocubes-based sensor,. *Sensors Actuators B Chem.* **2022**, *362*, 131737.

(36) Li, Y.-X.; et al. Hierarchical morphology-dependent gas-sensing performances of three-dimensional $SnO_2$ nanostructures,. *ACS sensors* **2017**, *2* (1), 102−110.

(37) Wang, Z.; Hou, C.; De, Q.; Gu, F.; Han, D. One-step synthesis of Co-doped $In_2O_3$ nanorods for high response of formaldehyde sensor at low temperature,. *ACS sensors* **2018**, *3* (2), 468−475.

(38) Shingange, K.; Swart, H. C.; Mhlongo, G. H. $H_2S$ detection capabilities with fibrous-like La-doped ZnO nanostructures: A comparative study on the combined effects of La-doping and post-annealing,. *J. Alloys Compd.* **2019**, *797*, 284−301.

(39) Zhang, D.; Wu, J.; Cao, Y. Cobalt-doped indium oxide/ molybdenum disulfide ternary nanocomposite toward carbon monoxide gas sensing,. *J. Alloys Compd.* **2019**, *777*, 443−453.

(40) Pi, M.; et al. Improved acetone gas sensing performance based on optimization of a transition metal doped $WO_3$ system at room temperature,. *J. Phys. D. Appl. Phys.* **2021**, *54* (15), 155107.

(41) Venkatesh, R.; et al. Analysis of optical dispersion parameters and electrochromic properties of manganese-doped $Co_3O_4$ dendrite structured thin films,. *J. Phys. Chem. Solids* **2018**, *122*, 118−129.

(42) Dhamodaran, M.; Karuppannan, R.; Murugan, R.; Boukhvalov, D. W.; Pandian, M. S.; Perumalsamy, R. Morphology Controlled Synthesis of Fe and Mn co-doped $In_2O_3$ Nanocubes and Their Dopant-Atom Effects on Electronic Structure and Magnetic Properties,. *J. Magn. Magn. Mater.* **2022**, *560*, 169547.

(43) Öztas, M.; Bedir, M. Thickness dependence of structural, electrical and optical properties of sprayed ZnO: Cu films,. *Thin Solid Films* **2008**, *516* (8), 1703−1709.

(44) Mhlongo, G. H.; et al. Room temperature ferromagnetism and gas sensing in ZnO nanostructures: Influence of intrinsic defects and Mn, Co, Cu doping,. *Appl. Surf. Sci.* **2016**, *390*, 804−815.

(45) Almontasser, A.; Parveen, A. Probing the effect of Ni, Co and Fe doping concentrations on the antibacterial behaviors of MgO nanoparticles,. *Sci. Rep.* **2022**, *12* (1), 7922.

(46) Deng, N.; Li, J.; Hong, B.; Jin, D.; Peng, X.; Wang, X.; Ge, H.; Jin, H. Nanocasting synthesis of Co-doped $In_2O_3$: a 3D diluted magnetic semiconductor composed of nanospheres,. *J. Nanoparticle Res.* **2015**, *17* (4), 1−11.

(47) Kgomo, M. B.; Shingange, K.; Nemufulwi, M. I.; Swart, H. C.; Mhlongo, G. H. Belt-like $In_2O_3$ based sensor for methane detection: Influence of morphological, surface defects and textural behavior,. *Mater. Res. Bull.* **2023**, *158*, 112076.

(48) Nemufulwi, M. I.; Swart, H. C.; Mhlongo, G. H. A comprehensive comparison study on magnetic behaviour, defects-related emission and Ni substitution to clarify the origin of enhanced acetone detection capabilities,. *Sensors Actuators B Chem.* **2021**, *339*, 129860.

(49) Shingange, K.; Swart, H.; Mhlongo, G. H. Ultrafast detection of low acetone concentration displayed by au-loaded $LaFeO_3$ nanobelts owing to synergetic effects of porous 1D morphology and catalytic activity of au nanoparticles,. *ACS omega* **2019**, *4* (21), 19018−19029.

(50) Mhlongo, G. H.; Motaung, D. E.; Cummings, F. R.; Swart, H. C.; Ray, S. S. A highly responsive $NH_3$ sensor based on Pd-loaded ZnO nanoparticles prepared via a chemical precipitation approach,. *Sci. Rep.* **2019**, *9* (1), 1−18.

(51) Ahammad, A. J. S.; et al. Porous tal palm carbon nanosheets: preparation, characterization and application for the simultaneous determination of dopamine and uric acid,. *Nanoscale Adv.* **2019**, *1* (2), 613−626.

(52) Arooj, S.; et al. Green emission of indium oxide via hydrogen treatment,. *RSC Adv.* **2018**, *8* (21), 11828−11833.

(53) Cao, H.; Qiu, X.; Liang, Y.; Zhu, Q.; Zhao, M. Room-temperature ultraviolet-emitting In$_2$O$_3$ nanowires,. *Appl. Phys. Lett.* **2003**, *83* (4), 761−763.

(54) Wang, S.; Cao, J.; Cui, W.; Fan, L.; Li, X.; Li, D. Oxygen vacancies and grain boundaries potential barriers modulation facilitated formaldehyde gas sensing performances for In$_2$O$_3$ hierarchical architectures,. *Sensors Actuators B Chem.* **2018**, *255*, 159−165.

(55) Anand, K.; Kaur, J.; Singh, R. C.; Thangaraj, R. Structural, optical and gas sensing properties of pure and Mn-doped In$_2$O$_3$ nanoparticles,. *Ceram. Int.* **2016**, *42* (9), 10957−10966.

(56) Kaleemulla, S.; Reddy, A. S.; Uthanna, S.; Reddy, P. S. Physical properties of In$_2$O$_3$ thin films prepared at various oxygen partial pressures,. *J. Alloys Compd.* **2009**, *479* (1−2), 589−593.

(57) Jothibas, M.; Manoharan, C.; Ramalingam, S.; Dhanapandian, S.; Bououdina, M. Spectroscopic analysis, structural, microstructural, optical and electrical properties of Zn-doped In$_2$O$_3$ thin films,. *Spectrochim. Acta Part A Mol. Biomol. Spectrosc.* **2014**, *122*, 171−178.

(58) Wei, H.-L.; Zhang, L.; Liu, Z.-L.; Yao, K.-L. Fabrication and photoluminescence characteristics of In$_2$O$_3$ nanohillocks,. *Chinese Phys. B* **2011**, *20* (11), 118102.

(59) Seetha, M.; Meena, P.; Mangalaraj, D.; Masuda, Y.; Senthil, K. Synthesis of indium oxide cubic crystals by modified hydrothermal route for application in room temperature flexible ethanol sensors,. *Mater. Chem. Phys.* **2012**, *133* (1), 47−54.

(60) Wang, Y.; et al. Enhanced NO$_2$ gas sensing properties based on Rb-doped hierarchical flower-like In$_2$O$_3$ microspheres at low temperature,. *Sensors Actuators B Chem.* **2021**, *332*, 129497.

(61) Liu, H.; Li, P.; Liu, B.; Zhang, T.; Zhang, Y. Au/La Co-Modified In$_2$O$_3$ Nanospheres for Highly Sensitive Ethanol Gas Detection,. *Chemosensors* **2022**, *10* (10), 392.

(62) Shingange, K.; Swart, H. C.; Mhlongo, G. H. Enhanced ethanol sensing abilities of fiber-like La$_{1−x}$Ce$_x$CoO$_3$ (0≤ x≤ 0.2) perovskites based-sensors at low operating temperatures,. *Sensors Actuators B Chem.* **2023**, *377*, 133012.

(63) Badadhe, S. S.; Mulla, I. S. H$_2$S gas sensitive indium-doped ZnO thin films: Preparation and characterization,. *Sensors Actuators B Chem.* **2009**, *143* (1), 164−170.

(64) Bai, J.; et al. Functionalization of 1D In$_2$O$_3$ nanotubes with abundant oxygen vacancies by rare earth dopant for ultra-high sensitive ethanol detection,. *Sensors Actuators, B Chem.* **2020**, *324*, 128755.

(65) Shingange, K.; Swart, H. C.; Mhlongo, G. H. Design of porous p-type LaCoO$_3$ nanofibers with remarkable response and selectivity to ethanol at low operating temperature,. *Sensors Actuators B Chem.* **2020**, *308*, 127670.

(66) Liu, X.; et al. Design of superior ethanol gas sensor based on indium oxide/molybdenum disulfide nanocomposite via hydrothermal route,. *Appl. Surf. Sci.* **2018**, *447*, 49−56.

(67) Wen, Z.; Tian-Mo, L. Gas-sensing properties of SnO$_2$-TiO$_2$-based sensor for volatile organic compound gas and its sensing mechanism,. *Phys. B Condens. Matter* **2010**, *405* (5), 1345−1348.

(68) Li, Z.; Dzenis, Y. Highly efficient rapid ethanol sensing based on Co-doped In$_2$O$_3$ nanowires,. *Talanta* **2011**, *85* (1), 82−85.

(69) Qin, Z.; et al. Highly sensitive alcohol sensor based on a single Er-doped In$_2$O$_3$ nanoribbon,. *Chem. Phys. Lett.* **2016**, *646*, 12−17.

(70) Montazeri, A.; Jamali-Sheini, F. Enhanced ethanol gas-sensing performance of Pb-doped In$_2$O$_3$ nanostructures prepared by sonochemical method,. *Sensors Actuators B Chem.* **2017**, *242*, 778−791.

(71) Fang, J.; Ma, Z.-H.; Xue, J.-J.; Chen, X.; Xiao, R.-P.; Song, J.-M. Au doped In$_2$O$_3$ nanoparticles: Preparation, and their ethanol detection with high performance,. *Mater. Sci. Semicond. Process.* **2022**, *146*, 106701.

(72) Chen, X.; Deng, N.; Zhang, X.; Li, J.; Yang, Y.; Hong, B.; Jin, D.; Peng, X.; Wang, X.; Ge, H.; Jin, H.; et al. Cerium-doped indium oxide nanosphere arrays with enhanced ethanol-sensing properties,. *J. Nanoparticle Res.* **2019**, *21* (4), 1−16.

(73) Yang, Z.; Zhang, D.; Chen, H. MOF-derived indium oxide hollow microtubes/MoS$_2$ nanoparticles for NO$_2$ gas sensing,. *Sensors Actuators B Chem.* **2019**, *300*, 127037.

(74) Chen, K.; et al. Surface functionalization of porous In$_2$O$_3$ nanofibers with Zn nanoparticles for enhanced low-temperature NO$_2$ sensing properties,. *Sensors Actuators, B Chem.* **2020**, *308*, 127716.

(75) Krishna, K. G.; Parne, S.; Pothukanuri, N.; Kathirvelu, V.; Gandi, S.; Joshi, D. Nanostructured metal oxide semiconductor-based gas sensors: A comprehensive review,. *Sensors Actuators A Phys.* **2022**, *341*, 113578.

(76) Zhang, Q.; Wang, S.; Fu, H.; Wang, Y.; Yu, K.; Wang, L. Facile design and hydrothermal synthesis of In$_2$O$_3$ nanocube polycrystals with superior triethylamine sensing properties,. *ACS omega* **2020**, *5* (20), 11466−11472.

(77) Jin, Z.; Wang, C.; Wu, L.; Liu, H.; Shi, F.; Zhao, J.; Liu, F.; Fu, K.; Wang, F.; Wang, Z.; Liu, J.; et al. Construction of Pt/Ce-In$_2$O$_3$ hierarchical microspheres for superior triethylamine detection at low temperature,. *Colloids Surfaces A Physicochem. Eng. Asp.* **2023**, *659*, 130738.

(78) Xu, Q.; et al. Near room-temperature triethylamine sensor constructed with CuO/ZnO PN heterostructural nanorods directly on flat electrode,. *Sensors Actuators B Chem.* **2016**, *225*, 16−23.

(79) Sun, J.; Wang, Y.; Song, P.; Yang, Z.; Wang, Q. Metal-organic framework-derived Cr-doped hollow In$_2$O$_3$ nanoboxes with excellent gas-sensing performance toward ammonia,. *J. Alloys Compd.* **2021**, *879*, 160472.

(80) Park, S.; Kim, S.; Sun, G.-J.; Lee, C. Synthesis, structure, and ethanol gas sensing properties of In$_2$O$_3$ nanorods decorated with Bi$_2$O$_3$ nanoparticles,. *ACS Appl. Mater. Interfaces* **2015**, *7* (15), 8138−8146.

(81) Yan, S.; et al. Chemiresistive ethanol sensors based on In$_2$O$_3$/ZnSnO$_3$ nanocubes,. *Sensors and Actuators Reports* **2022**, *4*, 100099.

(82) Wu, X.; et al. Hydrothermal synthesis of flower-like Cr$_2$O$_3$-doped In$_2$O$_3$ nanorods clusters for ultra-low isoprene detection,. *Colloids Surfaces A Physicochem. Eng. Asp.* **2021**, *620*, 126606.

(83) Han, B.; et al. Hydrothermal synthesis of flower-like In$_2$O$_3$ as a chemiresistive isoprene sensor for breath analysis,. *Sensors Actuators B Chem.* **2020**, *309*, 127788.